

The Auditory Mechanics of the Outer Ear of the Bush Cricket: A Numerical Approach

Emine Celiker,^{1,*} Thorin Jonsson,^{2,3} and Fernando Montealegre-Z^{1,*}

¹University of Lincoln, School of Life Sciences, Joseph Banks Laboratories, Lincoln, United Kingdom; ²School of Biological Sciences, University of Bristol, Bristol, United Kingdom; and ³Institute of Biology, Karl-Franzens-University Graz, Graz, Austria

ABSTRACT Bush crickets have tympanal ears located in the forelegs. Their ears are elaborate, as they have outer-, middle-, and inner-ear components. The outer ear comprises an air-filled tube derived from the respiratory trachea, the acoustic trachea (AT), which transfers sound from the mesothoracic acoustic spiracle to the internal side of the ear drums in the legs. A key feature of the AT is its capacity to reduce the velocity of sound propagation and alter the acoustic driving forces of the tympanum (the ear drum), producing differences in sound pressure and time between the left and right sides, therefore aiding the directional hearing of the animal. It has been demonstrated experimentally that the tracheal sound transmission generates a gain of ~15 dB and a propagation velocity of 255 ms⁻¹, an approximately 25% reduction from free-field propagation. However, the mechanism responsible for this change in sound pressure level and velocity remains elusive. In this study, we investigate the mechanical processes behind the sound pressure gain in the AT by numerically modeling the tracheal acoustic behavior using the finite-element method and real three-dimensional geometries of the tracheae of the bush cricket *Copiphora gorgonensis*. Taking into account the thermoviscous acoustic-shell interaction on the propagation of sound, we analyze the effects of the horn-shaped domain, material properties of the tracheal wall, and the thermal processes on the change in sound pressure level in the AT. Through the numerical results obtained, it is discerned that the tracheal geometry is the main factor contributing to the observed pressure gain.

SIGNIFICANCE It has been shown that the bush-cricket ear is unique among insects because it performs similar biophysical mechanics as the mammalian ear, showing outer-, middle-, and inner-ear components for sound capturing, impedance conversion, and frequency analysis. This research focused on the outer ear, using for the first time, to our knowledge, three-dimensional geometries of the acoustic trachea (bush-cricket ear canal) and numerical methods to demonstrate the mechanism of passive sound amplification. Numerical results show that the spatial pressure distribution inside the acoustic trachea is similar to the distribution observed in the ear canal of mammals. This suggests a case of convergent evolution in which a respiratory structure (the trachea) evolved as an exponential horn to amplify and deliver sound pressure waves to a tympanal organ.

INTRODUCTION

The ears of bush crickets are located in the tibiae of the forelegs and are typically adapted to be most sensitive to sounds that are significant for reproductive success and/or survival (1). These are tympanal ears, which are endowed with outer-, middle-, and inner-ear components (2) (see Fig. 1). Each ear has two tympana (ear drums) that are formed from thin regions of leg cuticle in contact with the walls of a modified leg trachea (3). The tympana

of each leg are backed by this air-filled tube, the acoustic trachea (AT), which runs through the leg, ending at a spiracle on the side of the thorax. The spiracle is the opening in the thorax, through which sound enters the AT. Unlike the majority of animals with tympanal ears, for bush crickets, the sound pressure acts on both the external and internal surfaces of the tympanic membranes (TMs) (3–9). The acoustic input enters the AT located in the leg through the acoustic spiracle on the thorax and is enhanced as it is transferred to the internal surface of the TM in the air-filled and narrowing tube. The AT is derived from the respiratory system of the insect and therefore is made of spiraled taenidia, which are of cuticle origin (Chapter 16 (8)).

Submitted July 5, 2019, and accepted for publication November 26, 2019.

*Correspondence: eceliker@lincoln.ac.uk or fmontealegrez@lincoln.ac.uk

Editor: James Keener.

<https://doi.org/10.1016/j.bpj.2019.11.3394>

Crown Copyright © 2019

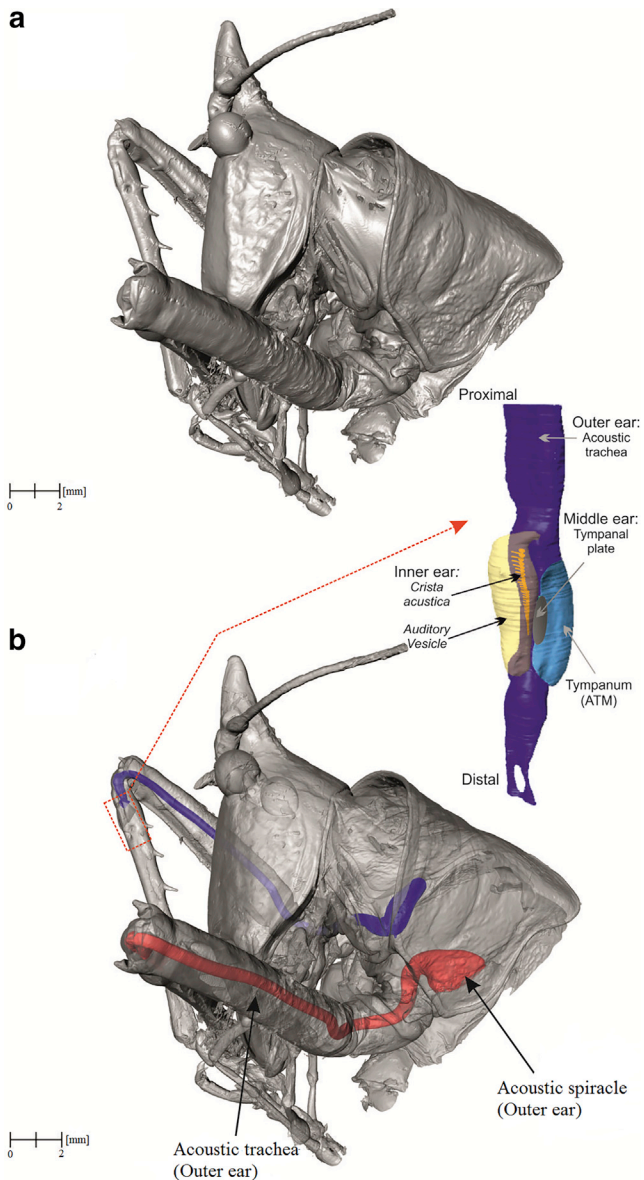


FIGURE 1 3D reconstruction of the head and thorax of a female *C. gorgonensis* obtained from μ -CT. (a) The external aspect of the body is shown; (b) a semitransparent version showing the location of the spiracle on the side of the thorax and the AT inside the thorax and front leg (outer ear) is given. Inset shows detail of the tympanal organ and middle- and inner-ear components; only the ATM is visible from this perspective. To see this figure in color, go online.

The size of the mesothoracic spiracle and trachea design vary across the known 7000 bush-cricket species, and for those species with large spiracles, the AT is the main sound input to the ears (4,5). For instance, the AT of the bush cricket *Copiphora gorgonensis* (Orthoptera: Tettigoniidae: Copiphorini) has an average length of 18 mm (6). At the spiracle end, the tracheal tube of this species is shaped like an exponential horn, and after a distance of 8 mm, the AT radius takes the mean value of $\sim 150 \mu\text{m}$ (6). The pipe extends forward from the thorax through into the fore

femoral cavity until it reaches the femorotibial joint (the knee), whereupon it enters the tibia and divides into two branches, an anterior branch feeding the anterior TM (ATM) and a posterior branch connected with the posterior TM (PTM) (2) (the ATM is shown in Fig. 1). Each tracheal branch leads to one tympanal membrane, and the dorsal part of the anterior branch harbors the auditory sensillae (known as the crista acustica (CA)). Dorsal to this area, between the two tympana on both sides of the tibia, lies the auditory vesicle, a fluid-filled cavity that encapsulates the CA. The CA and auditory vesicle represent the inner ear of the bush cricket where frequency analysis takes place. Both tracheal divisions merge again below the tympanal membranes, where the trachea narrows and ends right beneath the ear. Each tympanal membrane is placed against the outer surface of these tracheal divisions, creating the only place in the system where both sides of the tracheal wall are coupled to the outside air.

Fig. 1 shows the AT of a female *C. gorgonensis* obtained through x-ray microcomputed tomography (μ -CT) scan and three-dimensional (3D) reconstruction.

The lumen of the AT is covered by an elastic wall, consisting of taenidia, and is filled with gas that is believed to be a mixture of air and gases internally produced by the animal such as carbon dioxide. The ears of the bush cricket are thought to act as pressure difference receivers, and because the sound reaches both surfaces of the TM, the ears become inherently directional (10). The internal version of the sound is passively amplified in the trachea, and thus, there are considerable differences in the amplitude of the sound arriving internally and externally (the internally arriving sound has an amplitude four times higher than the externally arriving sound because of the passive amplification inside the AT), from which the bush crickets benefit with directional hearing (11). These differences become more pronounced as the sound arriving internally propagates with lower velocity than sound arriving externally (6). Consequently, the correct measurement of the sound pressure and velocity in the AT lateral to the TM becomes important for understanding the directional hearing mechanism of the bush cricket.

It has been suggested from experimental results that the increase in the magnitude of the sound pressure acting on the internal sides of the TM is due to the AT functioning as an exponential horn (7,12). Even though mathematical models explaining horn theory have been proposed as early as 1919 by Webster (see (13,14) and references therein), on a complex domain such as the AT, the exact solution of this problem is not known. Nonetheless, to our knowledge, no attempt to find an approximate solution to this problem on the real 3D AT geometry has been undertaken. Using 3D geometries of the AT of male and female *C. gorgonensis* obtained by μ -CT scanning and by the application of the finite-element method (FEM), this work investigates the mechanism of passive acoustic amplification in the AT.

MATERIALS AND METHODS

μ -CT description and segmentation

For the numerical simulations, the domain was taken as the left and right AT of one male and one female *C. gorgonensis*. This species is endemic to the island of Gorgona, Colombia, located off the southwestern Colombian Pacific coast, and was brought to the UK under the research permit granted by the Colombian Authority. Specimens were collected as nymphs in their natural habitat and maintained in captivity in cages at 25°C, a light/dark cycle of 11/13 h and 70%, where they were fed on a mix of pollen and dry cat food until they reached adulthood.

The specimens were initially used for various laser experiments, as described in (6). They survived these experiments, and we waited for their natural deaths before using them for μ -CT scanning. However, they were freshly dead for this process and were preserved in Bouin's solution during the short time before scanning. This procedure has been approved under the ethics regulations of the University of Lincoln, under the project entitled The Insect Cochlea, Ethics Reference 2019-May-0160.

The geometry of the bush-cricket AT was obtained using x-ray μ -CT and 3D reconstruction, using standard biomedical imaging software and the same procedure outlined in (6). Complete animals were scanned with a Bruker Skyscan 1272 (microCT; Bruker, Kontich, Belgium) at 100 kV, 36 μ A with a 0.5-mm-thick aluminum filter, resulting in a voxel size of 11 μ m. The reconstruction of the AT was carried out with AMIRA (v. 6.7.0; Thermo Fisher Scientific, Waltham, MA), and the results were imported into Comsol, v 5.4 (15), as STL files for further processing.

Mathematical model

For the mathematical model, we take into account the fact that when sound propagates in domains with small dimensions such as the AT, the sound waves become attenuated because of thermal and viscous losses. More specifically, the losses occur in the acoustic thermal and viscous boundary layers near the walls (16). Furthermore, when the wall of the domain has an elastic structure, the interaction of the sound waves with the elastic wall also needs to be taken into account to model the propagation of sound precisely.

This complex mechanism is most accurately represented through the set of equations governing the thermoviscous acoustic-shell interaction. This set of equations models the thermal conduction effects and viscous losses explicitly and solves for the acoustic perturbations in pressure, velocity, and temperature in the fluid, as well as the velocity of elastic waves in the wall.

We let \mathcal{Q} denote the domain of the mathematical model, which is the AT described above, and \mathcal{Q}_f , \mathcal{Q}_s denote the fluid and shell domains, respectively, where \mathcal{Q}_f is enclosed in the lumen of the AT, \mathcal{Q}_s is the wall surrounding the lumen, and $\mathcal{Q} = \mathcal{Q}_f \cup \mathcal{Q}_s$. Further, $\gamma = \mathcal{Q}_s \cap \mathcal{Q}_f$ is the interface at the lumen surfaces of the wall and the wall boundaries of the fluid; γ_1 denotes the acoustic spiracle, which is the open end of the tube; γ_2 , which is the distal end, contains the TM; and γ_3 is the outer wall of the shell.

The governing equations representing the propagation of sound in \mathcal{Q}_f are the fully linearized Navier-Stokes equation, the continuity equation, and the energy conservation equation. The solution to these equations is assumed to be time harmonic, so we solve for the spatial dependence of the amplitudes of the primary unknowns. We will also assume adiabatic thermal processes for the system and hence consider the solution of the following system of equations:

$$i\omega\rho + \nabla \cdot (\rho_0 \mathbf{u}_f) = 0, \quad (1)$$

$$i\omega\rho\mathbf{u}_f = \nabla \cdot \left[-pI + \mu \left(\nabla \mathbf{u}_f + (\nabla \mathbf{u}_f)^T \right) - \left(\frac{2\mu}{3} - \mu_B \right) (\nabla \mathbf{u}_f) I \right], \quad (2)$$

$$T = \frac{\alpha_0 T_0}{\rho_0 C_p} p, \quad (3)$$

where Eq. 1 is the continuity equation, Eq. 2 is derived from the linearized Navier-Stokes equations, and Eq. 3 is derived from the energy equation; ω = angular frequency; ρ = density; $\rho_0(p_0, T_0)$ = equilibrium density; μ = dynamic viscosity; μ_B = bulk viscosity; C_p = heat capacity at constant pressure; T_0 = equilibrium temperature; p_0 = equilibrium pressure; I = identity matrix and α_0 = coefficient of thermal expansion; and the dependent variables p = pressure, \mathbf{u}_f = velocity, and T = temperature in the fluid. The values of the parameters ρ_0 , μ , μ_B , C_p , and α_0 are obtained from the properties of the fluid.

In addition to these, we also take into account the linearized equation of state, which relates variations in pressure, temperature, and density

$$\rho = \rho_0(\beta_T p - \alpha_0 T), \quad (4)$$

where β_T is the isothermal compressibility obtained from the speed of sound in the considered fluid.

At the spiracle γ_1 , we assume the following conditions hold:

$$p = p_{bnd}, \quad (5)$$

$$\begin{aligned} \left[-pI + \mu \left(\nabla \mathbf{u}_f + (\nabla \mathbf{u}_f)^T \right) - \left(\frac{2\mu}{3} - \mu_B \right) (\nabla \mathbf{u}_f) I \right] \\ \times \mathbf{n} = -p_{bnd} \mathbf{n}, \end{aligned} \quad (6)$$

where Eq. 5 is the amplitude of the harmonic pressure source and \mathbf{n} is the normal vector.

On γ_2 , there is an impedance of magnitude Z_0 representing the specific acoustic impedance of the TM, and the equation

$$\begin{aligned} \left[-pI + \mu \left(\nabla \mathbf{u}_f + (\nabla \mathbf{u}_f)^T \right) - \left(\frac{2\mu}{3} - \mu_B \right) (\nabla \mathbf{u}_f) I \right] \\ \times \mathbf{n} = -Z_0 (\mathbf{u}_f \cdot \mathbf{n}) \cdot \mathbf{n} \end{aligned} \quad (7)$$

is satisfied.

Next, we consider the equations for modeling the propagation of time-independent harmonic waves in the elastic wall. We make the assumption that the AT wall is built of isotropic, incompressible, and homogeneous material. This is done by the Navier-Cauchy equation given below, which models the mechanical properties in the structure \mathcal{Q}_s assuming small deformations (17):

$$-\rho_s \omega^2 \mathbf{U}_s - \nabla \cdot \sigma(\mathbf{U}_s) = 0, \quad (8)$$

where ρ_s is the density of the wall and the components of the stress tensor $\sigma(\mathbf{U}_s)$ are

$$\sigma_{ij} = \frac{E}{1+\nu} \epsilon_{ij} + \frac{E\nu}{(1+\nu)(1-2\nu)} \epsilon_{kk} \delta_{ij}, \quad i, j = 1, 2, 3, \quad (9)$$

with E = Young's modulus; ν = Poisson's ratio, $0 < \nu < 1/2$; $\epsilon_{ij} = (1/2)((\partial U_{si}/\partial x_j) + (\partial U_{sj}/\partial x_i))$, the strain tensor; and δ_{ij} the Kronecker-delta function. The dependent variable \mathbf{U}_s represents the displacement vector in \mathcal{Q}_s .

We also specify the boundary condition

$$\sigma_{ij} \times n_j = 0, i, j = 1, 2, 3 \text{ on } \gamma_3, \quad (10)$$

so that there is no external stress on the wall.

Finally, at the interface γ_3 , which is where the defined fluid and shell systems are coupled, the following equations hold:

$$\mathbf{u}_f = i\omega \mathbf{U}_s, \quad (11)$$

$$-n \times (-k\nabla T) = 0, \quad (12)$$

where k = thermal conductivity and the complex number $i = \sqrt{-1}$.

It is well known that damping is also often present in biological systems. Hence, a Rayleigh damping defined as in (18) is assumed to be present in the system because of the AT wall. Rayleigh damping that is usually used for proportional damping systems linearly connects the damping matrix to the mass and stiffness matrices. This assumption, together with the orthogonality condition of the vibration modes, results in the following relation between the damping ratio ξ_i and the natural frequencies ω_i of an undamped system:

$$\xi_i = \frac{\alpha_{dM}}{2\omega_i} + \frac{\omega_i \beta_{dK}}{2}, \quad (13)$$

where α_{dM} and β_{dK} are the mass proportional and stiffness proportional Rayleigh damping coefficients, respectively.

For running the simulations, we use mean values for the mass damping parameter α_{dM} and the stiffness damping parameter β_{dK} based on the values presented in (18).

Numerical method

The variational form of the introduced equations, along with the defined boundary conditions, are solved with the FEM using the commercial software Comsol Multiphysics v.5.4 (15). By the application of Green's theorem (Chapter 5 in (19)), only the first-order derivatives of the dependent variables (p , \mathbf{u}_f , T , \mathbf{U}_s) are present under the variational form so that the C_0 (conforming) FEM can be used to solve the problem.

The finite-element mesh is formed in the AT after an artificial boundary is formed on γ_1 so that a closed volume is obtained for the domain. An artificial boundary is also placed on γ_2 that models the TM.

For the approximate solution of the variational problem, the 3D finite-element mesh is constructed in the domain Ω_f with the use of tetrahedral elements and boundary layers in the vicinity of the boundary of the domain. The tetrahedral elements are chosen such that each element K satisfies the following inequality:

$$\text{diam}(K) \leq \frac{\text{wavelength of sound wave}}{30}. \quad (14)$$

In general, it is accepted that ~ 10 elements per wavelength will suffice for a reasonable finite-element approximation of the propagation of a soundwave. We further reduce the size of our elements to account for the complex geometry of the domain (see Fig. 2). Using finer meshes did not make any difference in the obtained results.

The tetrahedral mesh is connected to the boundary layer mesh, which is employed near the boundary of the domain to resolve the thermal and viscous boundary layers encountered, as depicted in Fig. 3. In total, five boundary layers are used, with the thinnest boundary layer having a width of $5 \mu\text{m}$ and the layers having a stretching factor of 1.2. This part of the mesh is formed of prisms.

Lastly, the finite-element mesh on Ω_s is formed using shell elements of the mixed interpolation of tensorial components type (20), which are suit-

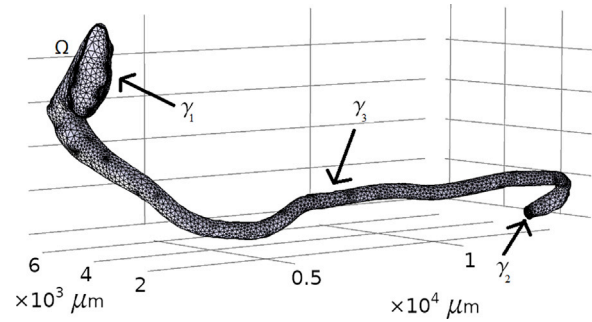


FIGURE 2 The finite-element mesh formed in the acoustic trachea for the approximation of the propagation of sound. To see this figure in color, go online.

able for effectively capturing different shell behaviors with varied and complex stress conditions.

The solution of the system of finite-element equations is based on quadratic Lagrange elements for all the dependent variables, and the outlined governing equations are solved using the 3D thermoviscous acoustic-shell interaction model of Comsol Multiphysics (15).

At the open end γ_1 of the AT, we assume that there is a plane wave entering the domain at a frequency in the range 1–80 kHz and with a sound pressure of ~ 85 dB, so that

$$p_{bnd} = 85 \text{ dB}$$

in Eqs. 5 and 6.

As demonstrated in Eq. 6, the length of the AT is ~ 18 mm. At the spiracle end, it has a radius of $\sim 450 \mu\text{m}$, which reduces to $\sim 150 \mu\text{m}$ at a distance of 8 mm from the spiracle and remains roughly constant until it reaches the TM. Hence, the radius is small enough to expect uniform plane waves. In the part of the AT with a uniform radius, it is suitable to assume that distributed acoustic impedance is present, which has the magnitude

$$Z_{ac} = \rho_0 c / S (\text{Pa} \cdot \text{s} / \text{m}^3),$$

where, because the fluid inside the tube is air, ρ_0 is the density of air, c is the propagation velocity of sound in air, and $S = \pi r^2$ is the cross-sectional area of the tube, with r the radius (see (21), p. 232).

For the acoustic impedance of the TM of the bush cricket *C. gorgonensis*, to our knowledge, the specific resistance and reactance values have not been obtained experimentally. Hence, to take into account the important effect of the TM impedance on the standing waves, we have assumed a distributed acoustic impedance on the TM as well. A treatment of this form was also applied for the theoretical results of the sound propagation inside the gerbil ear canal in (22).

It is known that for conditions with constant values over a given surface area S , the specific impedance and the acoustic impedance are related by

$$Z_{sp} = S Z_{ac}. \quad (15)$$

It follows from Eq. 15 that the specific acoustic impedance

$$Z_{sp} = S \times (\rho_0 c / S) = \rho_0 c (\text{Pa} \cdot \text{s} / \text{m})$$

inside the tube.

For the sensitivity analysis of the system, we have varied the value of Z_0 in Eq. 7 to analyze the effect of the TM impedance on the sound propagation inside the AT, taking $Z_0 > Z_{sp}$.

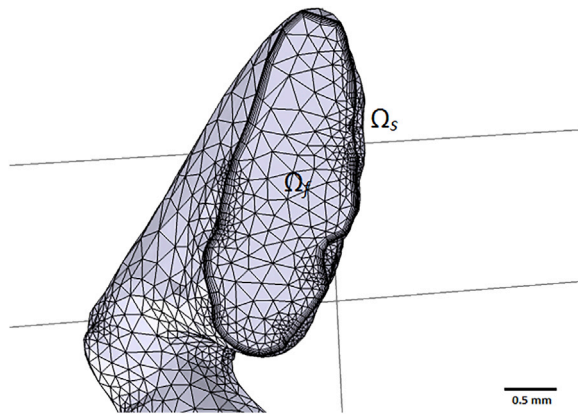


FIGURE 3 The finite-element mesh formed in the fluid domain, with boundary layer meshes adjacent to the wall for the approximate solution in the viscous and thermal boundary layers of the analytical solution and tetrahedral elements in the remainder of the domain, viewed from the spiracle γ_1 . To see this figure in color, go online.

RESULTS

Through numerical simulations, we demonstrate the pressure gain in the AT for a wide frequency range of the initial sound stimulus. For the boundary conditions (5,6), we let $p_{bnd} = 85$ dB and let the sound stimulus have a frequency in the interval 1–80 kHz, which is the hearing range of *C. gorgonensis*, with a resolution of 2048 Hz. Table 1 presents the parameters used while running the simulations, which are outlined in more detail below. Unless stated otherwise, the results presented are from the left trachea of a female *C. gorgonensis*. The results obtained from the right trachea of the same specimen and a male specimen are analogous to the results presented and are provided in Figs. S1–S15.

Spatial pressure variation

As demonstrated in Fig. 4, through numerical results, it is ascertained that the pressure distribution in the AT varies along the tube in a manner dependent on the frequency of the initial stimulus. At lower frequencies (i.e., 1000–2500 Hz), because of the wavelength of the sound being much greater than the average length of the AT, the distribution of sound near the tube is expected to be nearly uniform, as is observed in Fig. 4 a. At high frequencies, however, sound pressure can vary considerably within the AT because, in general, sound pressure variations along a tube of length L can become significant at frequencies at which the sound wavelength $\lambda < 10 L$ (21).

At frequencies for which λ is greater than $10 L$, spatial variations in sound pressure within the AT are small, so the sound pressure can be measured at any point within the tube. However, at higher frequencies, sound pressure is expected to vary substantially longitudinally along the

TABLE 1 Parameters Used in the Numerical Simulation of the Propagation of Sound in the AT of the Bush Cricket *C. gorgonensis*

Parameter	Value
Fluid	air
SPL at γ_1 , p_{bnd}	85 dB
Normal impedance of TM, Z_0	8000 Pa · s/m
AT wall, Young's modulus, E	1.7 GPa
AT wall, Poisson's ratio, ν	0.3
AT wall, density, ρ_s	1300 kg/m ³
Rayleigh damping	$\alpha_{dM} = 568.9 \text{ s}^{-1}$; $\beta_{dK} = 6.7 \times 10^{-7} \text{ s}$
AT wall thickness	11 μm
Equilibrium temperature, T_0	293.15 K
Equilibrium pressure, p_0	1 atm

AT, making it more challenging to obtain the pressure lateral to the TM.

Moreover, it was demonstrated in (23) that at high frequencies, the spatial pressure distribution is very sensitive to the curvature of the tube and the variation of the cross-sectional area along its length. The incident wave, which is of the form of a plane sound wave with frequency f , will be partly reflected when it encounters the walls of the AT, where the direction and the magnitude of the reflected wave will depend on the curvature of the wall and the diameter of the cross-sectional area. The reflected wave travels

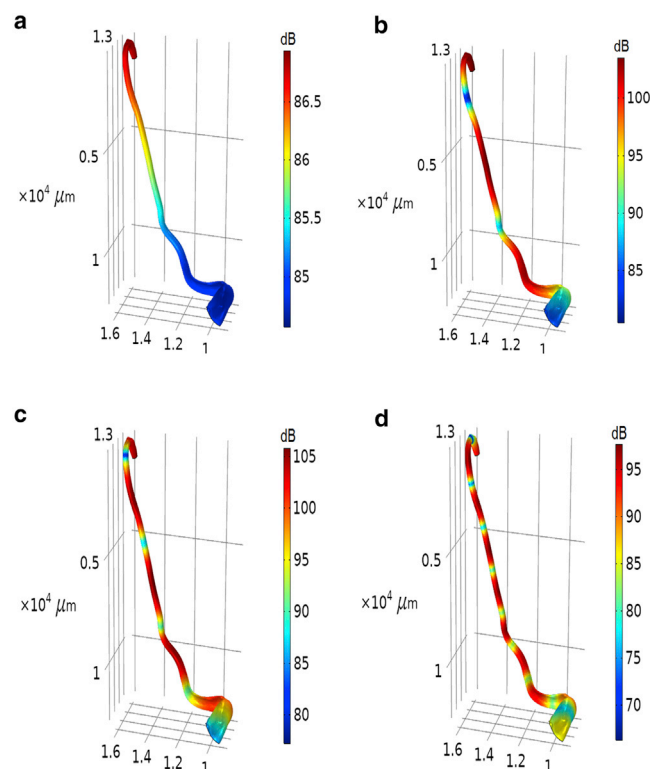


FIGURE 4 Spatial distribution of pressure in the left AT of a female *C. gorgonensis* with a plane wave sound stimulus of amplitude 85 dB and frequencies (a) 1 kHz, (b) 23 kHz, (c) 40 kHz, and (d) 79 kHz. To see this figure in color, go online.

backward along the AT with a phase shift so that the resulting sound field in the AT is the sum of the sound pressures of the incident and reflected waves.

Spatial variations in sound pressure as described above have been observed in the ear canals of the gerbil ear (22), the human ear (23,24), and the cat ear (25). Through the numerical results, similar behavior can also be observed in the AT of the bush cricket *C. gorgonensis*, shown in Fig. 4, highlighting further that the AT has similar behavior to the mammalian ear canal. From the results in Fig. 4, it can be observed that the sound wave is predominantly reflected from the TM end of the tube. An analogous pressure distribution is also present in the right AT of the female *C. gorgonensis*, which is demonstrated in Fig. S1, and in the left and right AT of a male *C. gorgonensis*, shown in Figs. S6 and S11, respectively.

We have also numerically calculated the viscous boundary layer thickness. From the results demonstrated in Fig. S16, it was observed that the thickness of the viscous boundary layer decreases as the frequency of the sound stimulus increases. It has the largest thickness of 69 μm at 1 kHz, and this reduces to ~ 10 μm at 80 kHz.

To further demonstrate the effect of the viscous losses, we compare our solutions to a numerical solution obtained from a system of equations that assumes no viscous losses. This is done by replacing Eqs. 1, 2, and 3 with the Helmholtz equation

$$\nabla^2 p + k^2 p = 0,$$

where $k^2 = (\omega/c)^2$. The results are demonstrated in Fig. S18, from which it can be observed that the pressure distribution inside AT is similar to the distribution in Fig. 4. However, there is a significant difference in the maximal value of pressure inside the tube.

The discrepancies in the results are further substantiated in Fig. S19, which demonstrates the magnitude of the sound pressure during sound transmission. When viscous losses are not emitted into the model, a pressure gain up to 30 dB can be observed during sound transmission, which does not agree with the experimental data (see Fig. S17 and (6)). Hence, the obtained numerical results suggest that viscous losses have an impact on the observed pressure gain.

Finally, in Fig. 5, we show the sound pressure distribution obtained at the distal end of the AT at a distance of 0.1 μm from the internal side of the TM for one female and one male *C. gorgonensis*, in the frequency range 1–80 kHz. From Fig. 5 a, it can be observed that the maximal pressure gain in the female AT is ~ 20 dB, which is obtained in the range 23–50 kHz. However, this gain is only observed in the left AT. Even though the pressure distributions in the left and right AT of the female specimen are similar, there is ~ 3 dB more gain in the left AT. The same pressure distribution is also obtained in the AT of the male specimen,

which is demonstrated in Fig. 5 b, with a gain of ~ 1 dB difference between the left and right tracheas. Interestingly, at 1 and 10 kHz, a small pressure loss is also present in the male AT (see Fig. 5 b). The slight differences between the pressure gain of the left and right AT can be attributed to the 3D reconstruction and the segmentation of the tracheal tubes, as well as the finite-element mesh constructed in the geometry.

Model sensitivity analysis

There are many mechanical phenomena involved in the propagation of sound in the AT. In this section, we consider the sensitivity analysis of the constructed model by taking into account the effect of the varying values of the parameters involved on the overall pressure gain. Keeping the remainder of the values in Table 1 the same, the consequences of altering the value of a parameter are investigated. The results are obtained by averaging the sound pressure level (SPL) obtained at four different points when the points are located at the distal end of the AT, at a distance of 0.1 μm from the artificial TM.

Background temperature

We start by investigating the outcome of varying the equilibrium temperature on the SPL in the AT, lateral to the TM. The obtained results, presented in Fig. 6 and Table 2, indicate that the background temperature does not have a significant effect on the observed pressure gain.

From Fig. 6, it can be observed that the distribution of SPL is relatively uniform throughout the frequency range 1–80 kHz. At lower frequencies (1–2 kHz), there is a slightly higher SPL when the temperature is lowered, with a difference of 4 dB at the peak in this range. In the remainder of the frequency range, however, the SPL range appears uniform, even though the distribution is shifted. Table 2 demonstrates the maximal SPL obtained in the considered frequency range, where it can be observed that there is a difference of 1.57 dB between the highest and lowest SPL obtained; nevertheless, there is no direct correlation between the background temperature and the change in SPL.

AT wall thickness

Through μ -CT measurements, it has been noted that the AT wall thickness ranges from 8 to 20 μm . The results presented in Fig. 7 show that for a very thin wall (for example, with a thickness of 0.5 μm), there is a significant pressure loss at the distal end of the AT. With a slight thickening of the AT wall to 2.5 μm , such a substantial pressure loss is no longer observed, and at 4 μm , it completely disappears. However, as observed through the μ -CT data, these are not realistic values for wall thickness. Interestingly, the thickness of the

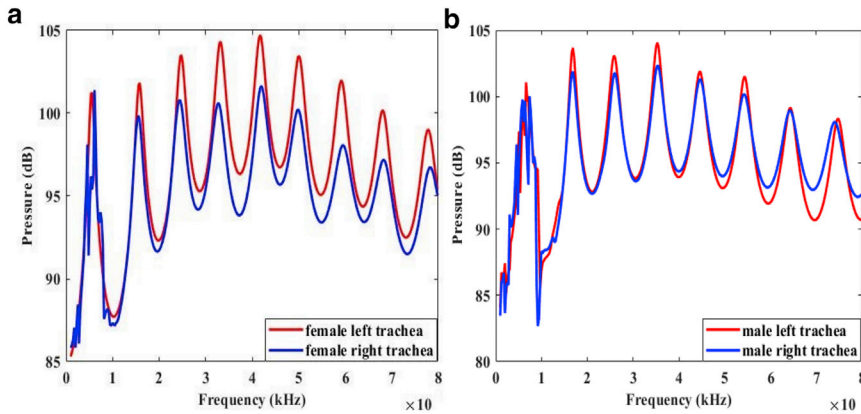


FIGURE 5 The sound pressure distribution at the γ_2 end of the left and right AT of (a) a female and (b) a male *C. gorgonensis* for an incident wave with amplitude 85 dB and a frequency in the range 1–80 kHz. To see this figure in color, go online.

AT wall does not have a significant effect on the pressure gain when it is of size $8 \mu\text{m}$ or more because the observed results in the range $8\text{--}30 \mu\text{m}$ are essentially identical. It is also noteworthy that in the higher frequencies ($60\text{--}80 \text{ kHz}$), there is less pressure gain regardless of the wall thickness.

AT wall material properties

To our knowledge, the material properties of the AT wall of the bush cricket *C. gorgonensis*—namely the Young's modulus E , Poisson's ratio ν , and density ρ_s —have not been investigated in detail. However, it is expected that the values of these parameters will be varying along the tube wall. In our model, we make the simplifying assumption that the elastic properties of the wall are isotropic. The values we adopted in Table 1 are based on the experimental results given in (26) for an American cockroach

(*Periplaneta americana*), where it has been demonstrated that the AT of this species has a mean value of 1.7 GPa and 0.3 for E and ν , respectively. We test the impact of the material properties of the AT wall on pressure gain in the ranges 1–20 GPa, 0–0.5, 1000–1300 kg/m^3 , for E , ν , and ρ_s , respectively, which are the values provided for insect cuticle in (27). The obtained results are presented in Fig. 8.

From Fig. 8a, it is observed that even though the variation in density has a slight effect on pressure gain in the frequency range 1–10 kHz, there is hardly any change when the frequency is between 10 and 80 kHz. Similarly, the results in Fig. 8, b and c demonstrate that the system is not sensitive to changes in Poisson's ratio or Young's modulus in the considered ranges.

The tympanum

The effect of the acoustic impedance of the TM on the pressure gain in the AT are shown in Fig. 9. Through the numerical results it was observed that for the expected pressure gain, the acoustic impedance of the tympanic membrane $Z_0 \geq 8000 \text{ Pa} \cdot \text{s/m}$. From Fig. 9, it can be further seen that the increase in Z_0 leads to small increases in pressure gain.

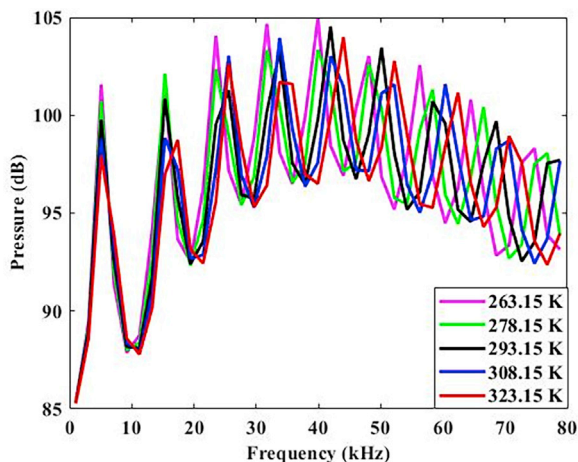


FIGURE 6 The effect of the background temperature on the pressure gain in the left AT of a female *C. gorgonensis*, lateral to the TM, with a plane wave sound stimulus of amplitude 85 dB and a frequency in the range 1–80 kHz. To see this figure in color, go online.

DISCUSSION

Comparing the numerical results obtained and the experimental results in (6), the conformity of the findings are evident. However, there are a few discrepancies in the experimental and numerical results that we would like to specify. In (6), the considered frequency range of the sound stimulus was 0–50 kHz, and it was observed that the maximal pressure gain was at 23–40 kHz. This is marginally different than the numerical results, in which the maximal gain is obtained in a wider interval of 23–50 kHz. Further, the response gain in (6), which was calculated from time domain and broadband measurements, ranged from 12 to

TABLE 2 The Maximal SPL for Various Background Temperatures at the Distal End of the Left AT of a Female *C. gorgonensis*

Temperature (K)	Frequency (Hz)	Maximal SPL (dB)
263.15	39,912	104.9164
278.15	39,912	103.3442
293.15	41,960	104.5333
308.15	33,768	103.9471
323.15	44,008	103.9833

16 dB. This is a smaller gain compared to the numerical results, in which the observed maximal pressure gain is 20 dB.

Hence, we highlight a few issues and discrepancies between the experimental and numerical setup that could account for the differences in the results. For instance, it is known that the elastic properties of the AT wall are not isotropic. However, this is not reflected in the input values used in the simulation because of the lack of experimental data, and the values used are based on the results of the tests on the AT of the American cockroach *P. americana* given in (26).

Even though in general, the system is believed to be governed by adiabatic thermal processes (which is also the condition implemented in the numerical simulations), from the discussion presented in (6) about the complex nature of the thermal mechanisms taking place in the AT, it follows that this might not always be the case. Based on the results obtained by Fletcher in (28), it was argued that because there is no definite cutoff stimulus frequency for the transition from isothermal to adiabatic processes, it is reasonable to assume that isothermal or a mixture of isothermal and adiabatic processes might also be taking place in the AT. We have also tested our system with the use of isothermal conditions, which requires changing Eq. 3 to

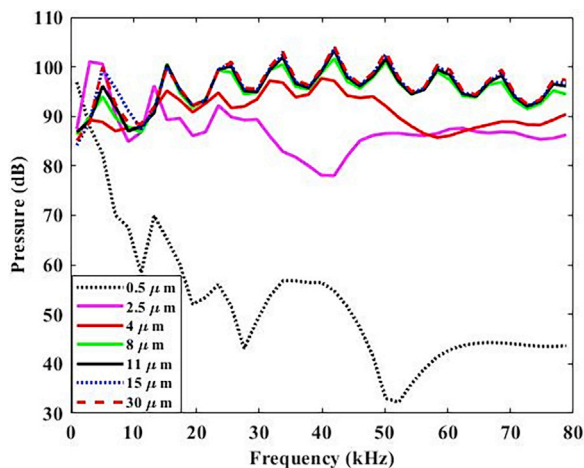


FIGURE 7 The sound pressure distribution for different values of AT wall thickness at the distal end of the left AT of a female *C. gorgonensis*, with a plane wave sound stimulus of amplitude 85 dB and a frequency in the range 1–80 kHz. To see this figure in color, go online.

$i\omega(\rho_0 C_p T - T_0 \alpha_0 p) = -\nabla(-k\nabla T)$, and at the interface, Eq. 12 is replaced by $T = 0$. In Fig. 10, we present the comparison of the results obtained for the sound pressure during transmission for an adiabatic and isothermal system, which shows that when isothermal processes take place in a system, there is less pressure gain during sound transmission.

Furthermore, it is worth noting that the complex geometry of the domain could have also contributed to the discrepancies in the results. In (6), the experiment was conducted while the specimen was mounted in a bespoke holder and placed in the acoustic free field. The forelegs were oriented forward, in a position akin to the bush cricket standing on a leaf. However, for the μ -CT image of the AT, it was not possible to obtain a similar position for the animal, and the leg was comparatively more bent at the knee of the specimen. This could lead to a variation in the standing waves occurring in the solution as a result of the reflected waves from the sharp bend, effecting the spatial distributions in sound pressure inside the tube.

Finally, we mention the effect of the Rayleigh damping coefficients defined in (13) on the pressure gain. For our mathematical model, we have taken into account the damping properties of the tracheal wall and neglected the damping of the TM. As stated in (29), there is no general agreement on α_{dM} and β_{dK} values for the damping of the TM, and there are studies in which it has been neglected completely (30). However, for the mammalian ear, it was shown that the TM has high damping properties (22). This argument was also supported in (30). Furthermore, the values of the damping coefficients we have applied at the AT wall are approximate and are not verified experimentally for the species *C. gorgonensis*. Hence, the damping effects can also account for the minor discrepancies observed between the experimental and numerical results.

Nevertheless, the numerical results obtained provide significant qualitative information about the role of the mechanical processes involved in pressure gain in the AT. Furthermore, the obtained results also enable us to make predictions about the pressure distribution inside the AT, which is inaccessible through experimentation. To obtain experimental evidence for the standing wave patterns, it would be required to open up the leg of the insect and place probe microphones along the AT. It would also be necessary to place a microphone at the TM end, which would not have the same acoustic impedance as the actual TM of the specimen. Hence, this would be a very invasive procedure and would not deliver reliable results because of the delicacy of the system.

For the experimental verification of our numerical results during sound transmission, in Fig. S17 we provide results obtained by us depicting the spectral range of the tracheal tube of a male *C. gorgonensis* as measured in the posterior tympanum. Our numerical results at the distal end of the AT have a distance of $\sim 5 \mu\text{m}$ from the TM; nevertheless, they are generally in accordance with the spectral range of the

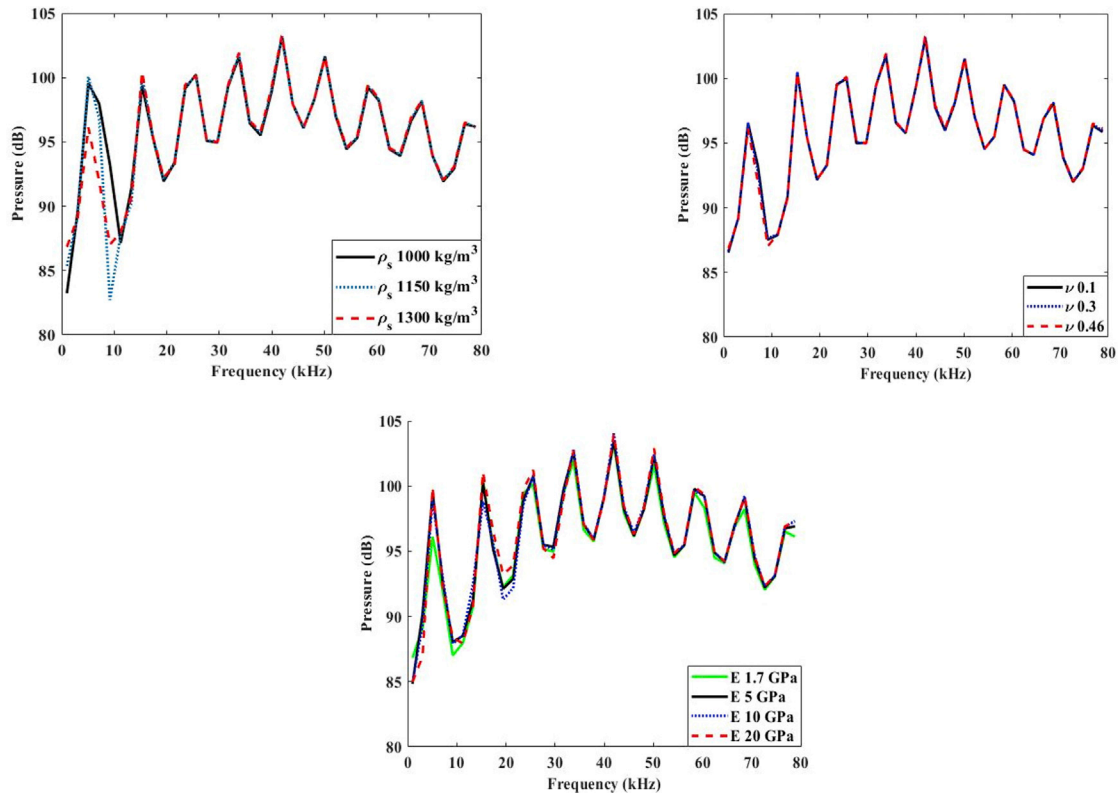


FIGURE 8 The variation of sound pressure at the distal end of the left trachea of a female *C. gorgonensis* for different values of (a) density ρ_s , (b) Poisson's ratio ν , and (c) Young's modulus E . The plane wave sound stimulus has amplitude 85 dB and a frequency in the range 1–80 kHz. To see this figure in color, go online.

experimental data, providing further affirmation of our numerical results.

Moreover, through the numerical results, the spatial pressure variation inside the AT was observed to be in accordance with the observation in the ear canal of mammals (22,23), further demonstrating the role of the tracheal tube as the equivalent of the ear canal for the bush cricket *C. gorgonensis*. From the sensitivity analysis of the model, the effects of the elastic properties, density, and the thickness of the AT wall on the pressure gain were also analyzed in detail; however, no significant effects of the properties of the wall were observed from the results of the numerical simulations.

Analyzing the effect of the acoustic impedance of the TM on the pressure gain also revealed that an increase in the impedance lead to an increase in the gain. However, a vast increase in the impedance parameter, Z_0 , would be needed to observe this, whereas for $Z_0 < 8000 \text{ Pa} \cdot \text{s/m}$, there is a more significant decrease in pressure gain as Z_0 decreases. Nonetheless, the simplifying assumption of representing the impedance of the TM with the distributed acoustic impedance, rather than applying a frequency-dependent acoustic impedance that takes into account the resistive and reactive properties of the TM, could also account for the discrepancies between the experimental and numerical

results. We have, however, investigated the effect of a complex valued impedance on the pressure amplitude during sound transmission, in which the value was based on the results in (31) for the mammalian ear. The results presented in Fig. S22 show that, apart from in the frequency range 1–10 kHz, there is no significant difference in the results. Nevertheless, we have not been able to define the impedance as a frequency-dependent value because of the lack of experimental data.

In (32), it was claimed that the resonant properties of the TM are not responsible for the tuning of the individual auditory receptors. This was used as a justification for the experiments carried out in (33), which involved the removal of the TM to test the tuning and intensity response characteristics of the auditory receptors in the CA. This notion, however, was criticized in (34), in which it was commented that the removal of the tympana opened the tracheal branches of the receptor organ to the outside air space, which brought the whole system to an acoustical shunt, thus preventing energy transfer to the receptors. They further claimed that the tympanal vibrations caused by the sound waves transmitted and amplified through the AT may be an important link in the transfer of energy by the acoustic structures of the CA.

In addition to the claims in (34), with the presented numerical results, we establish another function of the TM,

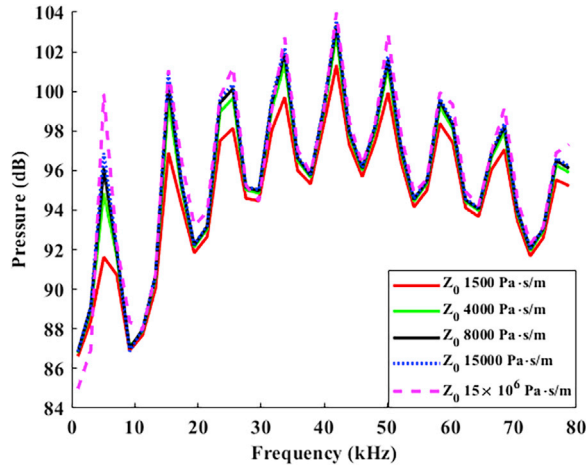


FIGURE 9 The variation of the SPL at the distal end of the left AT of a female *C. gorgonensis* for different values of the impedance of the tympanum with the plane wave sound stimulus of amplitude 85 dB and a frequency in the range 1–80 kHz. To see this figure in color, go online.

namely acting as the moderator of the gain in the tracheal tube. Consequently, as well as an acoustical shunt (34), their removal may also result in a change in pressure gain, thus impacting the transfer of energy of the CA.

Finally, based on the results of the sensitivity analysis, we conclude that the observed pressure gain in the AT heavily depends on the exponential horn-shaped structure of the tube. Even though there are some suggestive changes in the pressure gain as the parameters are varied for the sensitivity analysis, these changes are not significant enough to account for the vast gain in the AT. Hence, our results point to the importance of the geometry of the tracheal tube for the observed pressure gain. To further verify this claim, we are currently analyzing the pressure gain in the AT of different species of bush crickets. Even though they also have horn-shaped geometries, there are considerable differences in their size and horn shapes (for instance, conical or parabolic horns). These results will appear in a subsequent manuscript.

As a justification of the necessity of a 3D AT model for realistic numerical results, we also compare our results to the solution obtained from an analytical one-dimensional (1D) horn equation (35). In 1919, Webster presented a solution to the 3D wave equation by simplifying it from a 3D to a 1D problem (13). He did this by assuming that the sound energy was uniformly distributed over a plane wavefront perpendicular to the horn axis and considering only motion in the axial direction (14). In (25), to take into account the complex geometry of the mammalian ear canal, Webster's horn equation was modified to allow for the possible variations in cross section and curvature. This is achieved by introducing a curved coordinate system at the center axis of the ear canal and by using the arc length s to define position. Hence, the equation is formulated as

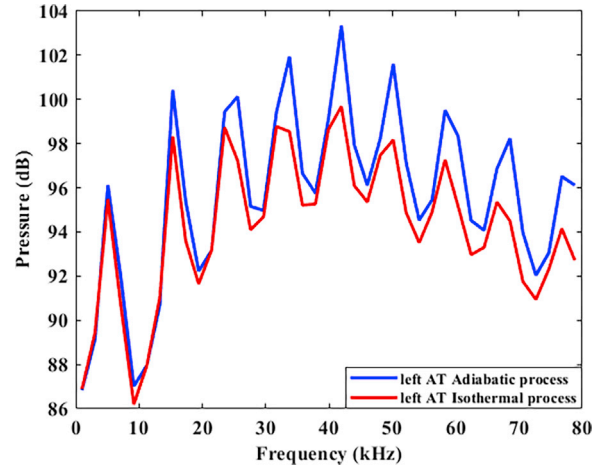


FIGURE 10 The pressure gain for the system with adiabatic and isothermal processes at the TM end of the left AT of a female *C. gorgonensis*, with an incident wave of amplitude 85 dB and a frequency in the range 1–80 kHz. To see this figure in color, go online.

$$\frac{d}{ds} \left(A(s) \frac{dp(s)}{ds} \right) + k^2 A(s) p(s) = 0, \quad (16)$$

where $A(s)$ is the cross-sectional area, k is the wavenumber, and p is the complex pressure. Equation 16 is the usual horn equation, with the difference that it is defined with respect to the curved s axis.

We consider the solution of Eq. 16 by taking into account the cross-sectional areas of the AT, which are circular, and the spiracle is assumed to be perpendicular to $s = 0$. The coordinates lying on the center axis and the radii of the circular cross sections were obtained from the μ -CT model using AMIRA. To have the results consistent with the 3D models, we let $p(0) = 85$ dB and at the TM end, we consider the normal impedance boundary condition

$$\frac{dp}{ds} = p(s_{TM}) \frac{i\omega}{Z_0},$$

where s_{TM} is the arc length at the TM and $Z_0 = 8000$ Pa · s/m in accordance with the 3D model.

We present the 3D surface plots and the 1D solution of the pressure obtained from the data of the same specimen in Figs. S11 and S20, respectively. Comparison between the graphs shows that the ripples in pressure amplitude are consistent in each of the results; however, there is a considerable difference between the magnitudes of the amplitude. In relation to the experimental data, the results obtained from the 1D model are not as realistic as the 3D model, which is expected because the 1D model is more suitable for a waveguide whose diameter does not change too rapidly along the coordinate axis and is considerably smaller than the wavelength (25). At the spiracle end, the AT diameter

changes rapidly, and the hearing range of the animal is 2–80 kHz, resulting in the wavelength of the sound stimulus being considerably smaller than the AT length at higher frequencies. Furthermore, the 1D model assumes a rigid wall and does not take viscous and thermal losses into account.

Another reason that could lead to discrepancies in the results is that in the 1D model, the sound wave is assumed to be uniform. However, looking at the cross sections of the results obtained in the 3D model in Fig. S21, it is evident that this is not always the case. Hence, the 1D model can be regarded as too simplistic for modeling the propagation of sound in the AT. Nevertheless, there is an agreement between the numerical results, which is further verification for the sound pressure distribution inside the AT because it is not possible to justify the variation experimentally.

CONCLUSIONS

As a result of the experimental findings in (6), which stated a gain of ~ 15 dB in the tracheal sound transmission of a *C. gorgonensis*, we numerically investigated the mechanical processes behind this phenomenon. This investigation was carried out with the use of the FEM and the 3D geometries of the tracheal tubes of one female and one male specimen. Through a model sensitivity analysis, it was observed that the material properties of the wall of the tracheal tube or the background temperature do not play a significant role in the pressure gain. Even though the change in the mechanical impedance of the TM was seen to have an effect on the pressure gain, the most important factor is the geometry of the AT, which is shaped like an exponential horn. In addition, through the numerical results, it was discerned that the spatial pressure distribution inside the AT is similar to the distribution observed in the ear canal (outer ear) of mammals, further establishing the function of the AT as the outer ear of the bush cricket *C. gorgonensis*.

SUPPORTING MATERIAL

Supporting Material can be found online at <https://doi.org/10.1016/j.bpj.2019.11.3394>.

AUTHOR CONTRIBUTIONS

T.J. carried out the segmentation and the model preparation. E.C. set up the mathematical model and ran all the simulations. F.M. conducted laser experiments to provide baseline data and is the project coordinator. All authors contributed to the analysis of the numerical data and the preparation of the article.

ACKNOWLEDGMENTS

The authors thank Prof. Paul Squires for his support and useful comments during the completion of this work.

This research is part of the project “The Insect Cochlea” funded by the European Research Council, Grant ERC-CoG-2017-773067 to F.M.Z. The specimens used in this study were exported under the research permit DTS0-G-090 14/08/2014 granted by the Colombian Authority. The conducted μ -CT scanning processes comply with the ethics regulations imposed by the University of Lincoln and have been approved as part of the project entitled “The Insect Cochlea,” Ethics Reference 2019-May-0160.

REFERENCES

- Lomas, K., F. Montealegre-Z, ..., D. Robert. 2011. Mechanical filtering for narrow-band hearing in the weta. *J. Exp. Biol.* 214:778–785.
- Montealegre-Z, F., T. Jonsson, ..., D. Robert. 2012. Convergent evolution between insect and mammalian audition. *Science*. 338:968–971.
- Bailey, W. J., and D. C. F. Rentz. 1990. *The Tettigoniidae: Biology, Systematics, and Evolution*. Springer-Verlag, Berlin.
- Bailey, W. J. 1993. The tettigoniid (Orthoptera: Tettigoniidae) ear: multiple functions and structural diversity. *Int. J. Insect Morphol. Embryol.* 22:185–205.
- Bailey, W. J. 1998. Do large bushcrickets have more sensitive ears? Natural variation in hearing thresholds within populations of the bush-cricket *Requena verticalis* (Listroscelidinae: Tettigoniidae). *Physiol. Entomol.* 23:105–112.
- Jonsson, T., F. Montealegre-Z, ..., D. Robert. 2016. Auditory mechanics in a bush-cricket: direct evidence of dual sound inputs in the pressure difference receiver. *J. R. Soc. Interface*. 13:20160560.
- Heinrich, R., M. Jatho, and K. Kalmring. 1993. Acoustic transmission characteristics of the tympanal tracheae of bushcrickets (Tettigoniidae). II: comparative studies of the tracheae of seven species. *J. Acoust. Soc. Am.* 93:3481–3489.
- Chapman, R. F. 1998. *The Insects: Structure and Function*. Cambridge University Press, Cambridge, UK.
- Larsen, O. N. 1981. Mechanical time resolution in some insect ears. *J. Comp. Physiol.* 143:297–304.
- Robert, D. 2005. Directional hearing in insects. In *Sound Source Localization*. A. N. Popper and R. R. Fay, eds. Springer, pp. 6–35.
- Michelsen, A., and O. N. Larsen. 2008. Pressure difference receiving ears. *Bioinspir. Biomim.* 3:011001.
- Michelsen, A., K. G. Heller, ..., K. Rohrseitz. 1994. A new biophysical method to determine the gain of the acoustic trachea in bushcrickets. *J. Comp. Physiol. A Neuroethol. Sens. Neural Behav. Physiol.* 175:145–151.
- Webster, A. G. 1919. Acoustical impedance and the theory of horns and of the phonograph. *Proc. Natl. Acad. Sci. USA*. 5:275–282.
- Kolbrek, B. 2008. Horn theory: an introduction, part 1. *Audio Xpress*. March:1–8.
- COMSOL AB. COMSOL Multiphysics v. 5.4.: COMSOL AB, Stockholm, Sweden. www.comsol.com.
- Malinen, M., M. Lyly, ..., L. Kärkkäinen. 2004. A finite element method for the modeling of thermo-viscous effects in acoustics. In *Proceedings of the European Congress on Computational Methods in Applied Science and Engineering (ECCOMAS 2004)*. P. Neittaanmäki, T. Rossi, K. Majava, and O. Pironneau, eds. ECCOMAS Council, pp. 1–12.
- Cummings, P., and X. Feng. 1999. Domain decomposition methods for a system of coupled acoustic and elastic Helmholtz equations. In *Eleventh International Conference on Domain Decomposition Methods*. Domain Decomposition Press, pp. 205–213.
- Rajabi, H., A. Shafiei, ..., S. N. Gorb. 2016. Effect of microstructure on the mechanical and damping behaviour of dragonfly wing veins. *R. Soc. Open Sci.* 3:160006.

19. Brenner, S., and R. Scott. 2007. *The Mathematical Theory of Finite Element Methods* Volume 15. Springer Science and Business Media, New York.
20. Bathe, K. J., A. Iosilevich, and D. Chapelle. 2000. An evaluation of the MITC shell elements. *Comput. Struct.* 75:1–30.
21. Kinsler, L. E., A. R. Frey, ..., J. V. Sanders. 1999. *Fundamentals of Acoustics*, Fourth Edition. Wiley-VCH, Weinheim.
22. Ravicz, M. E., E. S. Olson, and J. J. Rosowski. 2007. Sound pressure distribution and power flow within the gerbil ear canal from 100 Hz to 80 kHz. *J. Acoust. Soc. Am.* 122:2154–2173.
23. Stinson, M. R. 1985. The spatial distribution of sound pressure within scaled replicas of the human ear canal. *J. Acoust. Soc. Am.* 78:1596–1602.
24. Stevens, K. N., R. Berkovitz, ..., D. M. Green. 1987. Calibration of ear canals for audiometry at high frequencies. *J. Acoust. Soc. Am.* 81:470–484.
25. Khanna, S. M., and M. R. Stinson. 1985. Specification of the acoustical input to the ear at high frequencies. *J. Acoust. Soc. Am.* 77:577–589.
26. Webster, M. R., J. J. Socha, ..., R. De Vita. 2015. Structure of tracheae and the functional implications for collapse in the American cockroach. *Bioinspir. Biomim.* 10:066011.
27. Vincent, J. F., and U. G. Wegst. 2004. Design and mechanical properties of insect cuticle. *Arthropod Struct. Dev.* 33:187–199.
28. Fletcher, N. H. 1974. Adiabatic assumption for wave propagation. *Am. J. Phys.* 42:487–489.
29. Vollandi, G., F. Di Puccio, ..., C. Carmignani. 2011. Biomechanics of the tympanic membrane. *J. Biomech.* 44:1219–1236.
30. Mikhael, C. S., W. R. J. Funnell, and M. Bance. 2005. Middle-ear finite element modelling with realistic geometry and a priori material-property estimates. *CMBES.* 28:Dec. 2005.
31. Hudde, H. 1983. Measurement of the eardrum impedance of human ears. *J. Acoust. Soc. Am.* 73:242–247.
32. Oldfield, B. P. 1985. Short communication the role of the tympanic membranes in the tuning of auditory receptors in Tettigoniidae (Orthoptera: Ensifera). *J. Exp. Biol.* 116:493–497.
33. Oldfield, B. P. 1982. Tonotopic organisation of auditory receptors in Tettigoniidae (Orthoptera: Ensifera). *J. Comp. Physiol.* 147:461–469.
34. Kalmring, K., E. Hoffmann, ..., M. Grossbach. 1996. The auditory-vibratory sensory system of the bushcricket *Polysarcus denticauda* (Phaneropterinae, Tettigoniidae) II. physiology of receptor cells. *J. Exp. Zool.* 276:315–329.
35. Stinson, M. R., and G. A. Daigle. 2005. Comparison of an analytic horn equation approach and a boundary element method for the calculation of sound fields in the human ear canal. *J. Acoust. Soc. Am.* 118:2405–2411.